



HAL
open science

Presence and properties of acoustic peaks near the nozzle of impinging rocket jets

Mathieu Varé, Christophe Bogey

► **To cite this version:**

Mathieu Varé, Christophe Bogey. Presence and properties of acoustic peaks near the nozzle of impinging rocket jets. *Acta Acustica*, 2022, 6, 10.1051/aacus/2022033 . hal-03761415

HAL Id: hal-03761415

<https://hal.science/hal-03761415>



Submitted on 26 Aug 2022

HAL is a multi-disciplinary open access archive for the deposit and dissemination of scientific research documents, whether they are published or not. The documents may come from teaching and research institutions in France or abroad, or from public or private research centers.

L'archive ouverte pluridisciplinaire **HAL**, est destinée au dépôt et à la diffusion de documents scientifiques de niveau recherche, publiés ou non, émanant des établissements d'enseignement et de recherche français ou étrangers, des laboratoires publics ou privés.



Presence and properties of acoustic peaks near the nozzle of impinging rocket jets

Mathieu Varé*  and Christophe Bogey 

Univ Lyon, École Centrale de Lyon, INSA Lyon, Université Claude Bernard Lyon I, CNRS, Laboratoire de Mécanique des Fluides et d'Acoustique, UMR 5509, 69134 Écully, France

Received 25 March 2022, Accepted 8 August 2022

Abstract – The presence and properties of acoustic peaks near the nozzle of impinging rocket jets have been investigated. Four jets at a Mach number of 3.1 impinging on a plate at a distance $L = 15r_0$, $20r_0$, $25r_0$ and $30r_0$ from the nozzle, where r_0 is the nozzle radius, have been computed using large-eddy simulations. In all cases, upstream-travelling pressure waves are generated by the jet impingement on the plate, with amplitudes decreasing with the nozzle-to-plate distance. The near-nozzle pressure spectra contain peaks, at frequencies not varying much with this distance. For $L \geq 20r_0$, the spectra are dominated by a low-frequency peak, whereas two additional high-frequency peaks emerge for $L = 15r_0$. The low-frequency peak is associated with the azimuthal mode $n_\theta = 0$, whereas the two other ones are due to strong components for modes $n_\theta \geq 1$. As for near-nozzle tones for free and impinging jets at lower Mach numbers, the peak frequencies fall close to the frequency bands of the upstream-propagating guided jet waves, showing a link between the peaks and the latter waves. Regarding the peak levels, they do not change significantly with the nozzle-to-plate distance for the low-frequency peak, but they decrease by 1.5 to 18 dB as the distance increases for the other peaks. Finally, for $L \geq 20r_0$, the near-nozzle peak frequency is close to that of the strongest shear-layer structures, indicating a connexion between the upstream noise and these structures. For $L = 15r_0$, a shock-leakage mechanism of a near-plate shock is found to generate the upstream noise.

Keywords: Jet noise, Impinging rocket jet, Acoustic peaks

1 Introduction

During the lift-off of a space launcher, the hot supersonic gases of the engines impinge on the launch area, which generates intense sound waves. These waves propagate to the launcher fairing, where they exert strong acoustic loads likely to damage the payload. The sound fields near the rocket structure thus require a specific attention from the aerospace industry, as highlighted in the review by Lubert *et al.* [1]. In order to characterize them, the impingement of the gases exhausted by the engines on the launchpad can be modeled as a jet impinging on a flat plate. Such a simplified set-up has been studied experimentally and numerically for high-subsonic jets [2–8]. Intense tones were reported in the pressure spectra close to the jet nozzle. Similar tones were later found for impinging supersonic jets at Mach numbers lower than 2 in experiments [9–14] and simulations [15–18]. They are generated by a feedback loop establishing between the nozzle and the plate, formed by downstream-propagating Kelvin–Helmholtz instability waves and upstream-propagating guided jet waves. More

recently, tones of weaker amplitude were also noticed in the vicinity of the nozzle of free ideally expanded jets at Mach numbers between 0.5 and 2 [19–21]. Their frequencies lie in the allowable frequency ranges of the upstream-propagating guided jet waves, highlighting a close link with these waves.

For impinging rocket jets at Mach numbers higher than 3, the presence of such peaks close to the nozzle is not obvious. It was not mentioned in references [22–24] reporting simulations of jets at Mach numbers from 3.1 to 3.66 impinging on a plate at a distance L between 30 and 40 nozzle radii r_0 from the nozzle. In a recent work by the authors dealing with a similar configuration [25], a broad peak was, however, noticed at a low frequency in the pressure spectra near the nozzle. Its frequency is located in the allowable bands of the upstream-propagating guided jet waves, which suggests the establishment of a feedback phenomenon. Nevertheless, the peak is large and has a low amplitude, which questions the existence of such a feedback. In addition, it is unclear if the absence of marked peaks in the near-nozzle pressure fields of impinging rocket jets is due to the high Mach number of the jets or to the large nozzle-to-plate distance considered.

*Corresponding author: mathieu.vare@ec-lyon.fr

In the present paper, the presence of acoustic peaks in the near-nozzle pressure fields of rocket jets impinging on a flat plate is examined by performing Large-Eddy Simulations (LES) of four overexpanded jets. The jets are at an exit Mach number M_e of 3.1 and a Reynolds number Re_D of 2×10^5 . They impinge on a plate located at a distance of $L = 15r_0, 20r_0, 25r_0$ or $30r_0$ from the nozzle. The nozzle- to-plate distances are shorter than those of previous works [22–25] in order to discuss the possible establishment of feedback mechanisms between the nozzle and the plate. The first objective is to study the effects of the nozzle-to-plate distance on the sound waves propagating in the upstream direction. For that, the jet flow and acoustic fields are described. The near-nozzle pressure spectra are notably scrutinized in order to detect the emergence of possible peaks. The second objective is to analyze the characteristics of the near-nozzle peaks. To this end, the azimuthal structure of the sound field in the near-nozzle region is revealed. The variations of the frequencies and amplitudes of the peaks with the nozzle-to-plate distance are described. The peak frequencies are also compared with the frequencies bands allowed for the upstream-propagating guided jet waves for the present jets according to a vortex-sheet model. Finally, the last objective is to investigate the noise generation mechanisms of the impinging rocket jets. For this, properties of the flow fields close to the impingement area, including velocity spectra and motions of near-plate shocks, are presented.

This paper is organized as follows. The jet parameters and numerical methods used in the LES are documented in Section 2. The results of the simulations are presented in Section 3. Finally, concluding remarks are given in Section 4.

2 Parameters

2.1 Jet parameters

The exhaust parameters of the present jets are identical to those of the jets considered in a recent work [25]. The geometric parameters are described using cylindrical coordinates (r, θ, z) . The jets have an exhaust Mach number $M_e = u_e/c_e$ of 3.1 and a Reynolds number $Re_D = u_e D/\nu_e$ of 2×10^5 , where u_e is the velocity, c_e is the sound speed, $D = 2r_0$ is the nozzle diameter and ν_e is the kinematic viscosity at the jet nozzle exit. The exhaust temperature T_e and pressure p_e are equal to 738 K and $0.63p_0$, where $p_0 = 10^5$ Pa is the ambient pressure. The jets impinge on a plate located at a distance $L = 15r_0, 20r_0, 25r_0$ or $30r_0$ from the nozzle exit. The distance of $L = 30r_0$ corresponds to that for the impinging jets in Varé and Bogey [25], whereas the other distances are shorter in order to discuss the presence of feedback phenomena. The jets are generated by a straight pipe nozzle of length $2r_0$, at the inlet of which Blasius boundary layer velocity profiles with a thickness of $0.15r_0$ are imposed. The boundary layer transition from a fully laminar to a disturbed state is triggered by adding vortical disturbances non-correlated in the azimuthal direction in the pipe at $z = -r_0$ [26]. The mean velocity profiles

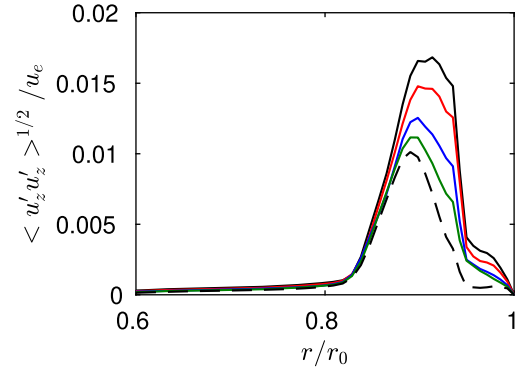


Figure 1. Nozzle-exit profiles of axial turbulence intensity $\langle u'_z u'_z \rangle^{1/2} / u_e$ for — $L = 15r_0$, — $L = 20r_0$, — $L = 25r_0$, — $L = 30r_0$, and - - - for the free jet [25].

obtained at the nozzle-exit $z = 0$ for the different jets are close to each other and very similar to those for the jets in Varé and Bogey [25]. The radial profiles of axial turbulence intensity $\langle u'_z u'_z \rangle^{1/2} / u_e$ at $z = 0$ are plotted in Figure 1 for the four impinging jets and for the corresponding free jet [25]. In all cases, they reach a peak at $r \approx 0.9r_0$. The peak value ranges between 1% and 1.6% of the exit velocity, indicating weakly disturbed nozzle-exit flow conditions. It is minimum for the free jet. For the impinging jets, it increases as the nozzle-to-plate distance is reduced, which suggests that the jet shear layers are disturbed by stronger upstream-propagating sound waves for shorter distances.

2.2 Numerical methods

The numerical set-up is identical to that used in previous works by the authors [8, 25]. In the simulations, the unsteady compressible Navier–Stokes equations are solved in cylindrical coordinates using an OpenMP based in-house solver. The time integration is performed using a six-stage Runge–Kutta algorithm and the spatial derivatives are evaluated with eleven-point low-dispersion finite-difference schemes [27] ensuring high accuracy down to five points per wavelength. At the end of each time step, grid-to-grid oscillations are removed by applying a selective filtering [28]. This filter also dissipates kinetic turbulent energy near the grid cut-off frequency, acting as a sub-grid-scale model [29]. Solid and adiabatic wall conditions are imposed at the nozzle and plate walls. In order to handle shock waves, a damping procedure using a dilatation-based shock detector and a second-order filter are used to remove Gibbs oscillations in the vicinity of shocks [28]. For $L \leq 25r_0$, to ensure the stability of the computation, this procedure is applied twice in the near-wall region for $r \leq 2r_0$ and $L - 2r_0 \leq z \leq L$. For the same reason, a standard fourth-order filter is also applied in this area for the cases $L = 15r_0$ and $L = 20r_0$. The radiation boundary conditions of Tam and Dong [30] are implemented at the radial and lateral boundaries of the computational domain. They are combined with sponge zones using grid stretching and Laplacian filtering to prevent significant spurious

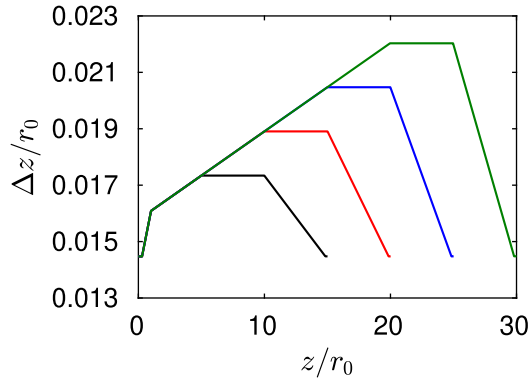


Figure 2. Variations of axial mesh spacing Δz for — $L = 15r_0$, — $L = 20r_0$, — $L = 25r_0$ and — $L = 30r_0$.

reflections. The singularity on the jet axis is removed by applying the method of Mohseni and Colonius [31].

2.3. Computational parameters

In the four simulations, the numbers of points in the radial and azimuthal directions are equal to $N_r = 501$ and $N_\theta = 256$, respectively. In the axial direction, the number of points N_z is equal to 1291 for $L = 15r_0$, 1531 for $L = 20r_0$, 1752 for $L = 25r_0$ and 1910 for $L = 30r_0$ yielding a total number of points between 170 and 250 millions. The grids extend out to $r = 15r_0$ in the radial direction and down to $z = L$ in the axial direction. The radial mesh grid used is identical to that in the LES of Varé and Bogey [25]. It notably enables a cut-off Strouhal number $St = fD/u_e$ of 1.62 for an acoustic wave discretized with five points per wavelength, where f is the frequency, in the jet near-acoustic field. The variations of the axial mesh spacing Δz are plotted in Figure 2. In all cases, the value of Δz is minimum and equal to $0.0144r_0$ at the nozzle exit and reaches its maximum value at $z = L - 10r_0$. This value is equal to $0.0173r_0$ for $L = 15r_0$, $0.019r_0$ for $L = 20r_0$, $0.0205r_0$ for $L = 25r_0$ and $0.022r_0$ for $L = 30r_0$. The mesh spacing is constant between $z = L - 10r_0$ and $z = L - 5r_0$, and finally decreases down to $\Delta z = 0.0144r_0$ at $z = L$.

The radial variations of the mesh spacing at $z = L$ on the plate in the wall-normal direction Δz^+ , in wall units, are represented in Figure 3 to discuss the discretization of the wall jet created by the jet impingement. This spacing is computed using the relation $\Delta z^+ = u_\tau \Delta z/\nu$, where u_τ is the mean friction velocity, Δz is the axial mesh spacing on the plate and ν is the kinematic viscosity. For all jets, it reaches a maximum value at a radial distance between $r = 0.5r_0$ and $r = r_0$. This value is equal to 23 for $L = 15r_0$ and decreases as the nozzle-to-plate distance is larger down to 15 for $L = 30r_0$. Farther from the axis, the dimensionless mesh spacing on the plate decreases for the four jets. It remains, however, much higher than 1, indicating that the turbulent boundary layer on the plate is not well resolved [32–35]. Nevertheless, the sound radiation of the wall jet is expected to be weak compared with that produced by the jet flow structures, as the wall jet velocity is significantly lower than the jet exhaust velocity.

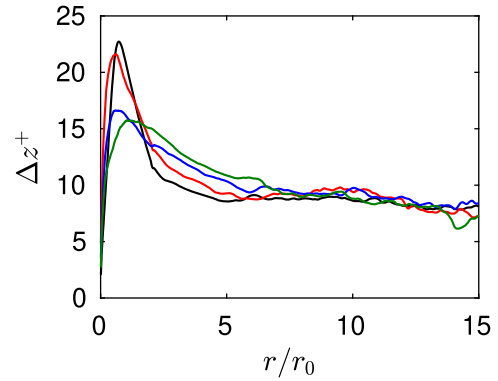


Figure 3. Variations of the axial mesh spacing Δz^+ on the plate, in wall units, for — $L = 15r_0$, — $L = 20r_0$, — $L = 25r_0$ and — $L = 30r_0$.

The results in the present paper are obtained for a simulation time of $1000r_0/u_e$. During the computations, density, the velocity components, pressure and their azimuthal Fourier coefficients up to the mode $n_\theta = 4$ are recorded on the same two-dimensional sections and at the same sampling frequencies as in Varé and Bogey [25]. These sections notably include the nozzle-exit plane at $z = 0$ and four planes at the azimuthal angles $\theta = 0, 90, 180$ and 270 degrees. The spectra presented below are calculated from these recordings and they are averaged in the azimuthal direction when possible. On the whole, 200,000 time steps were performed for each jet, consuming a total of 130,000 CPU hours, using 32 core nodes of Intel 6142 Skylake with a clock frequency of 2.6 GHz.

3 Results

3.1 Snapshots of the flow and acoustic fields

Fields of temperature and pressure fluctuations obtained inside and outside of the flow, respectively, are represented in Figure 4. In the temperature fields, diamond patterns typical of shock cells are present in the four jets downstream of the nozzle exit. The cells are progressively dampened by the turbulent mixing for $z \geq 10r_0$. Wall jets are created by the impingement of the flow on the plate. Zones of high temperature are also found in the impingement area. In this region, the temperature decreases as the nozzle-to-plate increases, indicating weaker jet-plate interactions for larger L .

In the pressure fields, waves originating from the impingement zone can be observed in the upstream direction. Their levels are typically of 3000 Pa for $L = 15r_0$ but are lower as the nozzle-to-plate distance increases. The wavefronts of two consecutive upstream-travelling sound waves are shown using red arrows for the nozzle-to-plate distances $L = 15r_0$ and $L = 25r_0$ in Figures 4a–4c to examine the frequency content of the upstream radiated noise. They are closer to each other for $L = 15r_0$ than for $L = 25r_0$, indicating stronger high-frequency components in the first case. For all jets, inclined wavefronts are also seen to travel

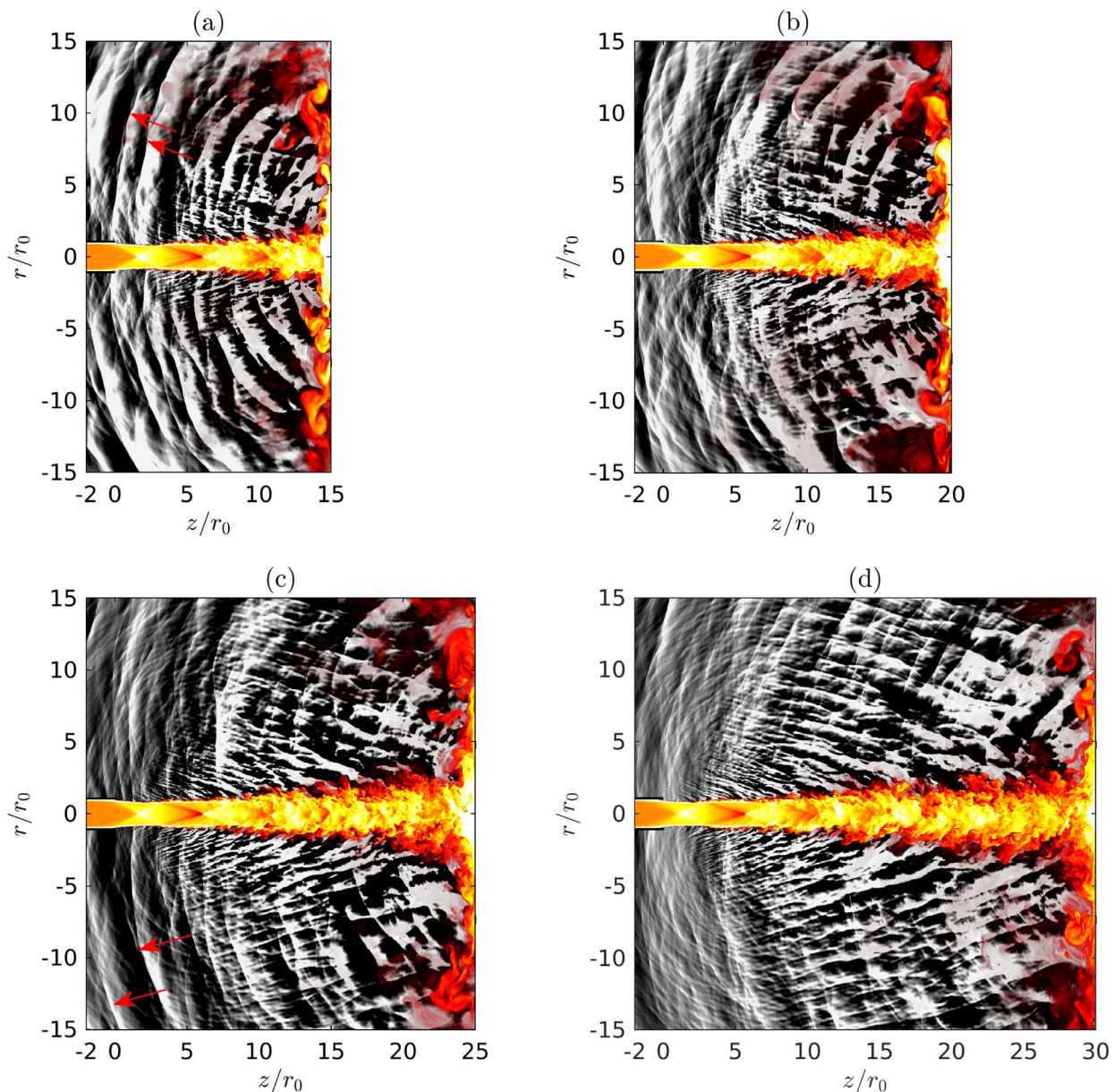


Figure 4. Snapshots in the (z, r) plane of temperature fluctuations in the flow and of pressure fluctuations outside for (a) $L = 15r_0$, (b) $L = 20r_0$, (c) $L = 25r_0$ and (d) $L = 30r_0$. The red arrows show the wavefronts of two consecutive upstream-propagating pressure waves for the nozzle-to-plate distances $L = 15r_0$ and $25r_0$. The color scales range from 0 to 780K for temperature, from red to white, and from -2000 to 2000 Pa for pressure, from black to white.

downstream. They are particularly noticeable for $z \geq 15r_0$ for $L = 25r_0$ and $L = 30r_0$ in Figures 4c and 4d. They are characteristic of Mach wave radiation, as noticed in previous simulations of jets at Mach numbers higher than 2 [36–39]. These waves are generated by turbulent coherent structures convected at a supersonic velocity.

3.2 Mean flow fields

The variations of the mean axial centerline velocity are represented in Figure 5a. The profiles obtained for the four jets are similar, suggesting that the nozzle-to-plate distance

has little effects on the mean velocity fields. Downstream of the nozzle, the axial velocity oscillates strongly, due to the presence of 3 to 6 shock cells depending on the nozzle-to-plate distance. In particular, the plate is located in the third cell for $L = 15r_0$, at the end of the fourth cell for $L = 20r_0$, in the sixth cell for $L = 25r_0$ and past the sixth cell for $L = 30r_0$. The amplitude of the oscillations decreases with the axial distance, because of the weakening of the cells by the turbulent mixing. The centerline velocity finally drops down to 0 at $z = L$. For the corresponding free jet, the end of the potential core, reached at the location z_c for which $\langle u_z \rangle / u_e = 0.9$, is found at $z_c = 15.7r_0$ in

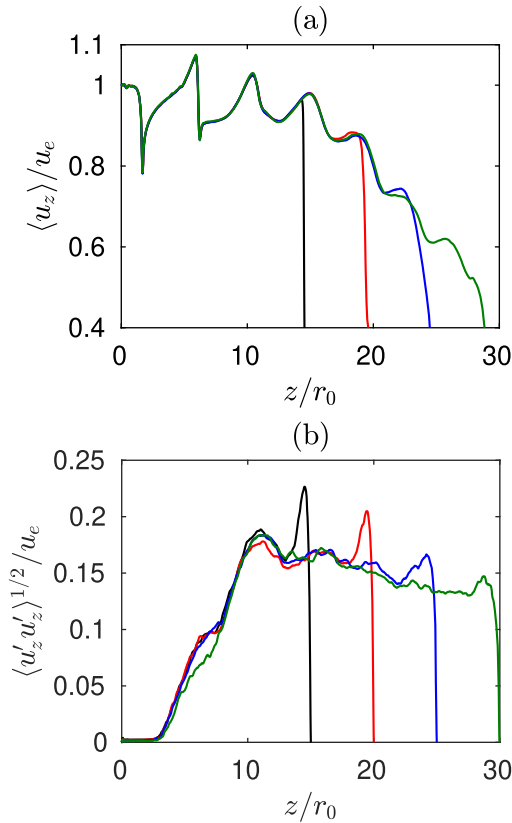


Figure 5. Variations of (a) the mean axial centerline velocity $\langle u_z \rangle / u_e$ and (b) the axial turbulence intensity $\langle u'_z u'_z \rangle^{1/2} / u_e$ at $r = r_0$ for — $L = 15r_0$, — $L = 20r_0$, — $L = 25r_0$ and — $L = 30r_0$.

Varé and Bogey [25]. Hence, the jet impinges on the plate before the end of the potential core for $L = 15r_0$ and after the latter in the three other cases.

The variations of the axial turbulence intensity in the shear layer at $r = r_0$ are plotted in Figure 5b. For all jets, the turbulence intensity remains below 1% from the nozzle exit down to $z = 2.5r_0$. Farther downstream, it increases sharply up to a peak value located around $z \approx 10r_0$, equal to about 18% for all nozzle-to-plate distances. Farther downstream, the rms values of the velocity fluctuations decrease with the axial distance and reach a second peak value close to the plate, before falling abruptly down to 0 at $z = L$.

3.3 Pressure spectra

The pressure spectra computed near the nozzle at $z = 0$ and $r = 2r_0$ are displayed as a function of the Strouhal number in Figure 6, along with the spectrum obtained for the free jet. For that jet, a peak centered around $St = 0.06$ is visible. It is linked to the broadband shock-associated noise (BBSAN) components produced by the interactions between the turbulent structures of the jet mixing layers and the shock cells [25]. For the impinging jets, the sound pressure levels are considerably higher than those for the free jet, by 5 to 22 dB depending on

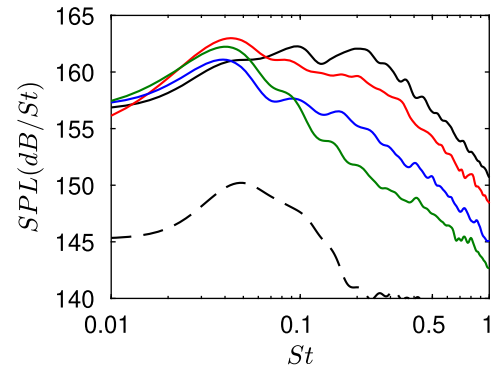


Figure 6. Sound pressure levels (SPL) at $z = 0$ and $r = 2r_0$ as a function of the Strouhal number St for — $L = 15r_0$, — $L = 20r_0$, — $L = 25r_0$ and — $L = 30r_0$ and - - - the free jet [25].

the nozzle-to-plate distance and the frequency. In that case, the noise generated by the jet impingement on the plate predominates strongly. For the three jets with $L \geq 20r_0$, the spectra all reach a peak at a Strouhal number of 0.04, with an amplitude which does not vary significantly with the nozzle-to-plate distance. In contrast, for $St \geq 0.1$, the sound levels increase as the plate is closer to the jet exit, and rise by approximately 3 dB for $L = 25r_0$ and by 7 dB for $L = 20r_0$ with respect to those for $L = 30r_0$. For $L = 15r_0$, the sound pressure spectrum is clearly different from the spectra for the three larger nozzle-to-plate distances. In particular, the high-frequency components for $St \geq 0.1$ are stronger by about 3 dB with respect to the case $L = 20r_0$, which is consistent with the pressure snapshots of Section 3.1. More importantly, the spectrum exhibits two additional peaks at $St = 0.09$ and 0.22 .

The variations of the overall sound pressure levels (OASPL) obtained at $z = 0$ and $r = 2r_0$ are represented as a function of the nozzle-to-plate distance in Figure 7. As expected, the levels are highest for $L = 15r_0$ and decrease with L , from 158.8 dB for $L = 15r_0$ down to 152.5 dB for $L = 30r_0$. Moreover, the levels for the largest nozzle-to-plate distance are 9.4 dB higher than those for the free jet, for which the value of L can be considered as infinite, showing that the impingement noise is significantly stronger than the mixing noise emitted by the free jet.

3.4 Properties of the near-nozzle peaks

To examine the azimuthal structure of the near-nozzle pressure fields, the contributions of the first four azimuthal modes to the pressure spectra at $z = 0$ and $r = 2r_0$ are shown in Figure 8 for $L = 15r_0$ and $L = 25r_0$. The results for the two other cases are not presented here because they are similar to those for $L = 25r_0$. The azimuthal decompositions for the two nozzle-to-plate distances in Figure 8 display similarities. Peaks can be observed at comparable frequencies. They are found at $St \approx 0.04$, 0.09 and 0.17 for $n_\theta = 0$, at $St \approx 0.08$ and 0.16 for $n_\theta = 1$, at $St = 0.2$ for $n_\theta = 2-3$ and at $St = 0.3$ for $n_\theta = 4$. For both jets, the axisymmetric mode is dominant for $St \leq 0.06$. As the

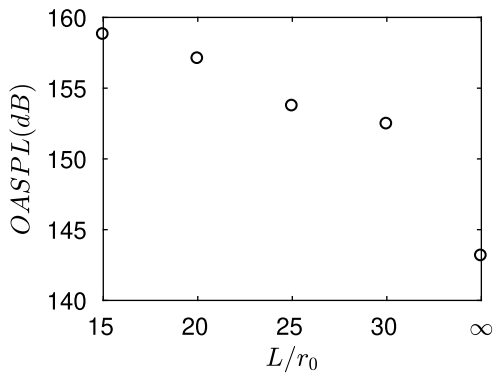


Figure 7. Overall sound pressure levels (OASPL) at $z = 0$ and $r = 2r_0$ as a function of the nozzle-to-plate distance.

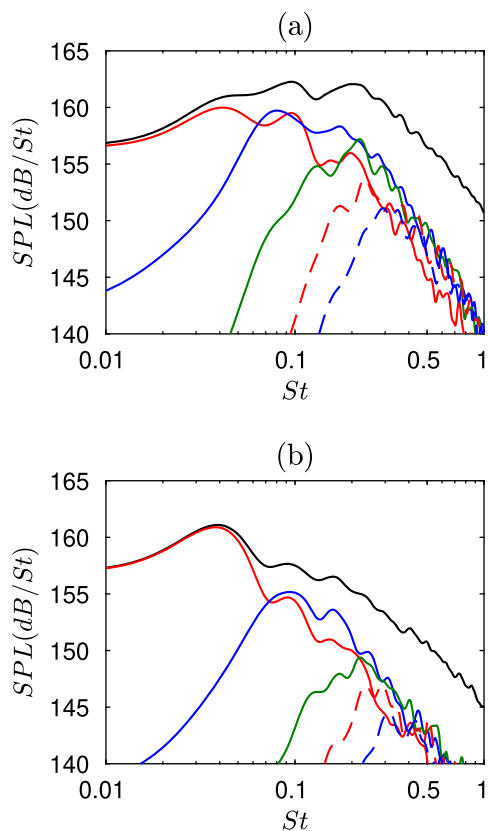


Figure 8. Sound pressure spectra at $z = 0$ and $r = 2r_0$ for (a) $L = 15r_0$ and (b) $L = 25r_0$: — full spectra and modes $n_0 = 0$, $n_0 = 1$, $n_0 = 2$, $n_0 = 3$ and $n_0 = 4$.

frequency increases, the contributions of modes $n_0 \geq 1$ become more significant. As a result, the levels for $n_0 = 1$ dominate for Strouhal numbers between 0.06 and 0.2, and the contributions of higher azimuthal modes to the pressure fields are notable for $St \geq 0.2$ for $n_0 = 2$ and for $St \geq 0.3$ for $n_0 = 3-4$. However, discrepancies are noted between the two nozzle-to-plate distances. For $L = 15r_0$, the peak at $St = 0.09$ for $n_0 = 0$ emerges 5 dB above that for $L = 25r_0$. The sound levels associated with the modes

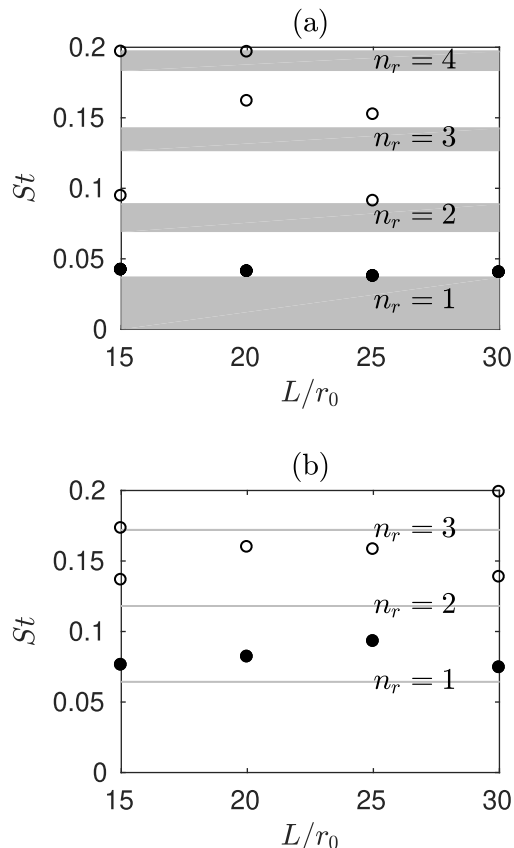


Figure 9. Strouhal numbers of the peaks in the near-nozzle pressure spectra as a function of the nozzle-to-plate distance for (a) $n_0 = 0$ and (b) $n_0 = 1$; \bullet dominant and \circ secondary peaks. The frequency bands of the upstream-propagating guided jet waves are in grey.

$n_0 \geq 1$ for $L = 15r_0$ are also stronger by about 5 dB than those for $L = 25r_0$ over the whole frequency range. In particular, the mode $n_0 = 1$ contributes strongly to the levels at $St = 0.09$ and the contributions of the modes $n_0 = 1$ and 2 are significant at $St = 0.22$, causing the emergence of two peaks in the full spectrum.

The variations of the Strouhal numbers of the near-nozzle peaks for the first two azimuthal modes are represented in Figure 9 as a function of the nozzle-to-plate distance. The allowable frequency ranges of the upstream-propagating guided jet waves obtained using a vortex-sheet model [40] are also displayed. These waves are organized in azimuthal and radial modes n_θ and n_r . For $n_\theta = 0$ in Figure 9a, the Strouhal number of the dominant peak does not vary much with the nozzle-to-plate distance. It is located very close to the upper band of the first radial mode of the guided jet waves, with $n_r = 1$, indicating a link with these waves. The secondary peaks are found at frequencies slightly higher than those of the bands for the second, third and fourth radial modes of the guided jet waves, with $n_r = 2$ to 4. The discrepancies observed between the LES and the vortex-sheet model may be due to the assumption of an infinitely thin shear layer in the model, leading to an underestimation of the frequencies of the guided jet

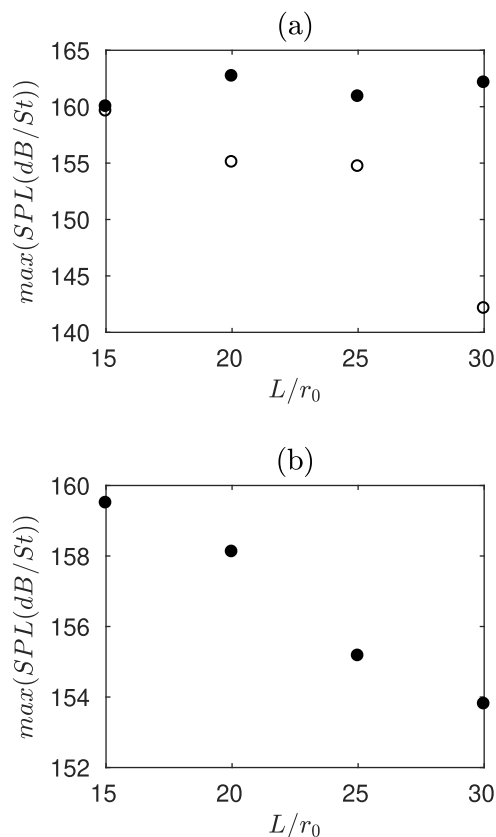


Figure 10. Levels of the peaks in the near-nozzle pressure spectra as a function of the nozzle-to-plate distance for (a) $n_\theta = 0$ and (b) $n_\theta = 1$; \bullet dominant and \circ secondary peaks.

waves [17]. For $n_\theta = 1$ in Figure 9b, the peak frequencies slightly vary with the nozzle-to-plate distance. They lie above the frequency bands of the first and second radial modes for the dominant and secondary peaks.

Finally, the variations of the amplitudes of the peaks with the nozzle-to-plate distance are plotted in Figure 10 for the first two azimuthal modes. For $n_\theta = 0$ in Figure 10a, the level of the dominant peak, associated with the guided jet mode $n_r = 1$, is close to 162 dB in all cases. On the contrary, for the secondary peak associated with $n_r = 2$, the peak amplitude decreases continuously with the nozzle-to-plate distance from 160 dB for $L = 15r_0$ down to 142 dB for $L = 30r_0$. For $n_\theta = 1$ in Figure 10b, the peak amplitude also decreases strongly with the distance. It is equal to 159 dB for $L = 15r_0$ but only to 154 dB for $L = 30r_0$. Therefore, the levels of the high-frequency peaks strongly depend on the nozzle-to-plate distance.

3.5 Velocity spectra

To link the sound spectra with the jet flow structures, the power spectral densities of the fluctuations of axial velocity obtained in the shear layer at $r = r_0$ between the nozzle exit and the plate are represented in Figure 11 for the four jet-to-plate distances. The frequencies of the peaks in the near-nozzle spectrum for $L = 15r_0$ are indicated by

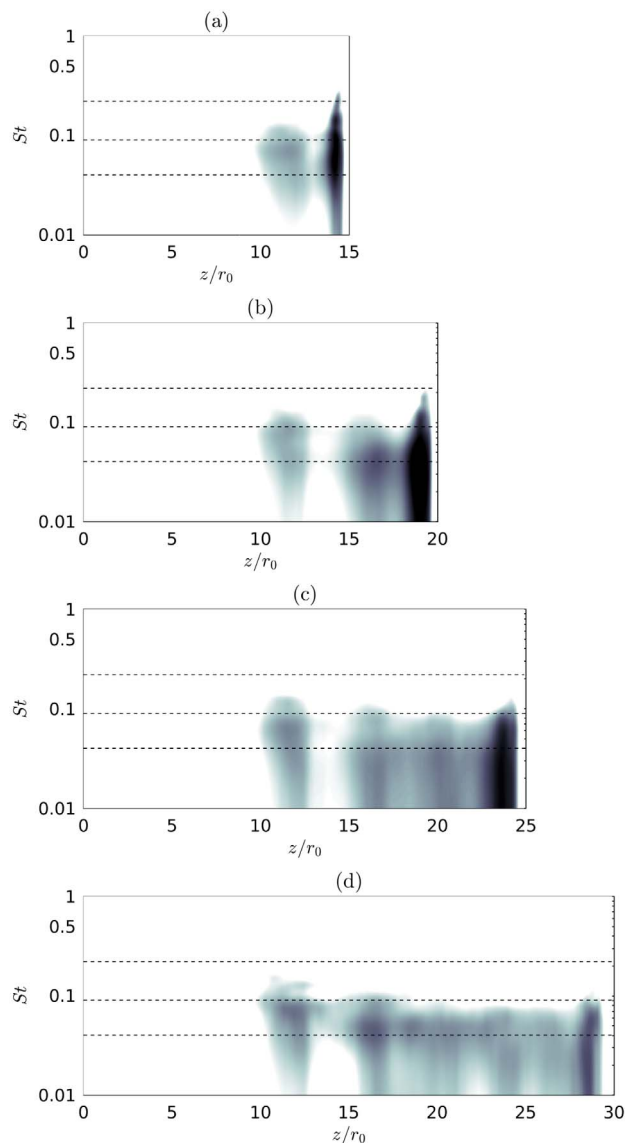


Figure 11. Power spectral densities of the fluctuations of axial velocity u'_z at $r = r_0$ between $z = 0$ and L for (a) $L = 15r_0$, (b) $L = 20r_0$, (c) $L = 25r_0$ and (d) $L = 30r_0$. The color scale is the same in the three cases and spreads over 3 dB, from white to black. The black dashed lines indicate the frequencies $St = 0.04$, 0.09 and 0.22 .

dashed lines. In all cases, the levels are very weak from the nozzle-exit plane down to $z = 10r_0$. These low levels can be explained by the fact that the shear layer is not centered on $r = r_0$ because of the overexpansion of the jets. Farther downstream, down to $z = L - 3r_0$, spots of significant energy are observed in the spectra for Strouhal numbers lower than 0.15. These low-frequency spots are related to large-scale vortical structures convected downstream. The frequencies of the peak components decrease with the axial distance. For example, for $L = 30r_0$ in Figure 11c, they vary from $St = 0.1$ at $z = 11r_0$ down to $St = 0.075$ at $z = 25r_0$. In all cases, close to the plate, the levels are especially strong. They are highest in a spot

around $z = L - r_0$, due to the flow impingement. High levels are found in these spots for Strouhal numbers below 0.3 for $L = 15r_0$, 0.2 for $L = 20r_0$ and 0.11 for $L = 30r_0$. Given that the jet structures are deviated in the wall jet a few radii upstream of the plate, these components can be expected to be linked to shocks or compressions near the plate rather than to the flow vortical structures.

Outside of the impingement area, the highest levels are found at $z_{\max} = 11.7r_0$ for $L = 15r_0$, $16.5r_0$ for $L = 20r_0$ and $L = 30r_0$ and $20.1r_0$ for $L = 25r_0$. To highlight the frequency contents of the most energetic flow structures, the velocity spectra obtained at these positions are shown in Figure 12. They reach their maximum value at a Strouhal number depending on the nozzle-to-plate distance. This Strouhal number is equal to $St = 0.07$ for $L = 15r_0$ and to $St = 0.03 - 0.04$ for $L \geq 20r_0$. The frequencies of the strongest flow structures are lower for the three largest nozzle-to-plate distances, because the jet potential core closes several nozzle radii upstream of the plate in these cases. For $L \geq 20r_0$, the peak frequency in the near-nozzle pressure spectra are close to those in the velocity spectra, suggesting a link between the most energetic flow structures and the near-nozzle pressure fields. However, for $L = 15r_0$, the peak frequency in the velocity spectrum is different from those in the near-nozzle sound spectra. In this case, the near-nozzle acoustic components may be not related to the strongest flow structures but to phenomena occurring in the impact zone such as shock leakage as discussed in what follows.

3.6 Sound generation near the plate

In order to examine the noise generation in the region of jet impingement, the fields of the axial gradient of density and of vorticity near the plate are represented in Figure 13 for $L = 15r_0$ and $L = 25r_0$. In the vorticity fields, in both cases, the turbulent structures of the shear layers impinge on the plate, creating a wall jet. Near the jet axis, for $L = 15r_0$ in Figure 13a, the level of vorticity is quite low, as the nozzle-to-plate distance is smaller than the size of the potential core for the free jet, whereas for $L = 25r_0$ in Figure 13b, vortical structures are found as the mixing layers have merged. In the density fields, for $L = 15r_0$ in Figure 13a, a normal shock is visible in the potential core just upstream of the plate at $z \approx 14.5r_0$, resulting from an intense impact of the jet flow on the plate. A similar near-plate shock was observed for jets at Mach numbers lower than 2 impinging on normal [11, 18, 41, 42] or inclined [43, 44] plates. The shock extends across the mixing layers, where it is curved in the upstream direction at $r = r_0$. The distortion of the shock tip is due to the interactions between the shock and the coherent structures of the shear layers. A part of the shock leaks out of the flow, which creates a circular sound wave visible around $z \approx 13.5r_0$ and $r_0 \leq r \leq 3r_0$. This sound generation mechanism, also involved in the production of screech noise [45–47], is referred to as shock leakage. It is shown here to be an efficient acoustic source in high-supersonic impinging jets in certain cases, as suggested by previous works [18, 41].

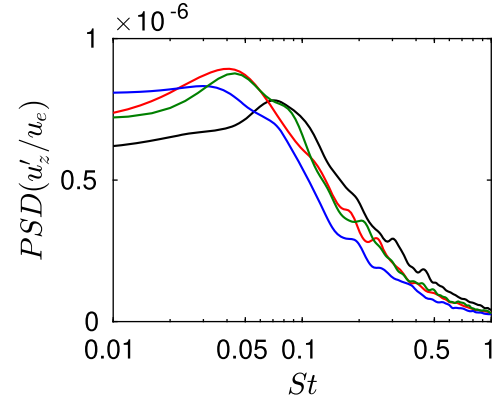


Figure 12. Power spectral densities of the fluctuations of axial velocity u'_z at $r = r_0$ and $z = z_{\max}$ for — $L = 15r_0$, — $L = 20r_0$, — $L = 25r_0$ and — $L = 30r_0$.

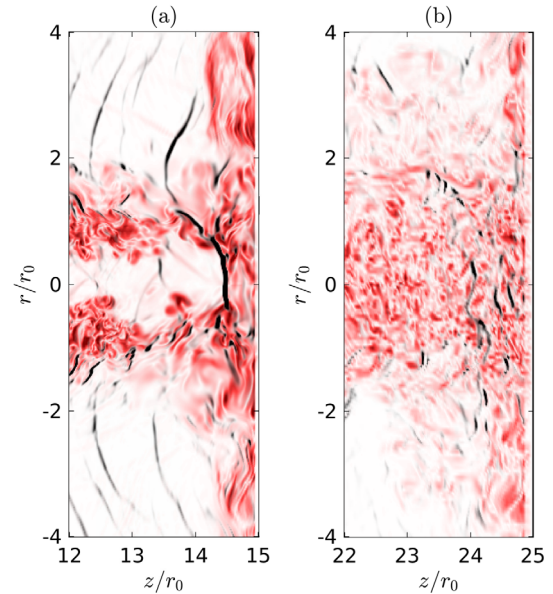


Figure 13. Fields of density gradient $\partial\rho/\partial z$ (black) and vorticity (red) near the plate for (a) $L = 15r_0$ and (b) $L = 25r_0$. The color scales range from 0 to $4\rho_0/r_0$ for the density gradient, from white to black, and from 0 to $7.5u_e/r_0$ for the vorticity, from white to red.

However, for $L = 25r_0$ in Figure 13b, no clear shock structure is present in the density field. The shock-leakage mechanism seems to be absent, which may explain the lower sound levels compared with the case $L = 15r_0$. The noise radiated in the upstream direction is produced by the impingement of vortical structures on the plate in that case.

To visualize the shock-leakage mechanism for the case $L = 15r_0$, the density gradient and vorticity fields near the plate are represented in Figures 14a–14e at times $t = 0$ to $10r_0/u_e$ in increment of $2.5r_0/u_e$. For $t = 0$ in Figure 14a, a near-plate shock is found on the axis around $z = 14.5r_0$. It extends across the mixing layer, where its tip is tilted in the upstream direction. Out of the mixing layer, a short line of strong density gradient is observed close to

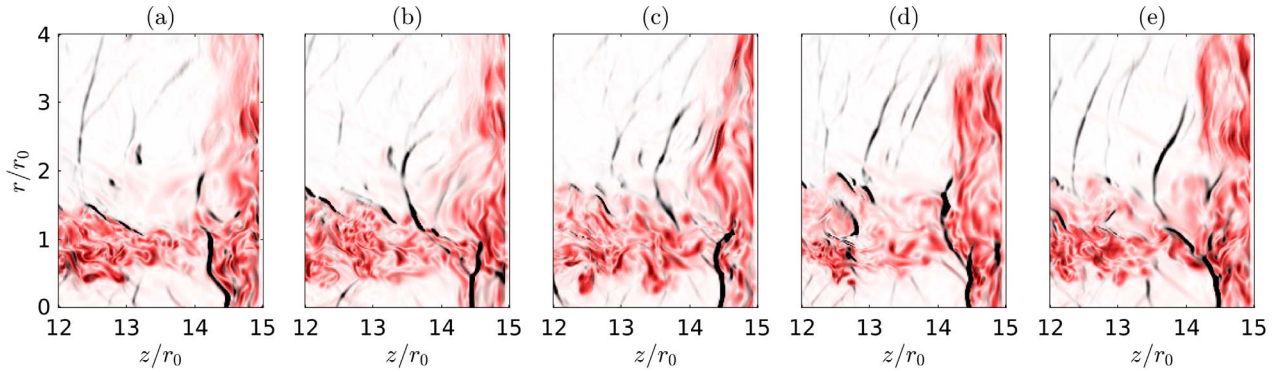


Figure 14. Fields of density gradient $\partial\rho/\partial z$ (black) and vorticity (red) near the plate for $L = 15r_0$ at (a) $t = 0$, (b) $t = 2.5r_0/u_e$, (c) $t = 5r_0/u_e$, (d) $t = 7.5r_0/u_e$ and (e) $t = 10r_0/u_e$. The color scales range from 0 to $4\rho_0/r_0$ for the density gradient, from white to black, and from 0 to $7.5u_e/r_0$ for the vorticity, from white to red.

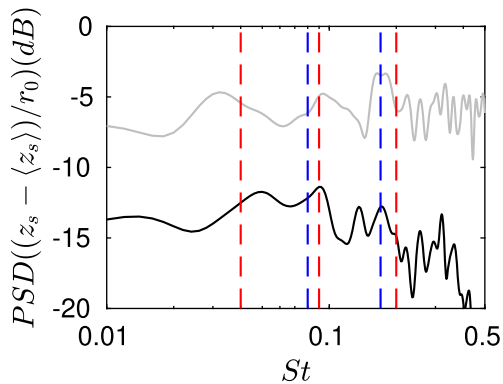


Figure 15. Power spectral densities of the axial oscillations of the near-plate shock for $L = 15r_0$ at — $r = 0$ and — $r = 0.85r_0$, and peak frequencies in the near-nozzle pressure spectra for — $n_\theta = 0$ and — $n_\theta = 1$.

the shock tip, at $z \approx 14.2r_0$ and between $r = r_0$ and $r = 2r_0$. This line is related to a pressure wave produced by the leakage of the shock out of the shear layer. For $t = 2.5r_0/u_e$ in Figure 14b, the normal shock moves downstream as it interacts with a vortical structure impinging on the plate. Its tip is slightly inclined towards the plate. Outside of the flow, the wave generated at $t = 0$ propagates up to $z \approx 13.7r_0$, which is consistent with the distance of $0.5r_0$ travelled by a sound wave between two snapshots. A second weak wavefront is also seen at $z \approx 14r_0$ and $r \approx 1.5r_0$, close to a coherent structure impinging on the plate. For $t = 5r_0/u_e$ in Figure 14c, the shock tip moves upstream and the sound waves produced previously propagate towards the nozzle. The shock tip is more and more curved in the upstream direction for $t = 7.5r_0/u_e$ and $10r_0/u_e$ in Figures 14d and 14e. For $t = 7.5r_0/u_e$ in Figure 14d, it extends in the radial direction up to $r = 1.5r_0$. Finally, for $t = 10r_0/u_e$ in Figure 14e, it leaks out of the shear layer, which creates a new sound wave outside the flow at $z \approx 13.5r_0$.

The motions of the near-plate shock for $L = 15r_0$ are studied using the methodology proposed by Gojon and Bogey [18] to investigate the oscillations of near-wall Mach

disks for underexpanded impinging jets. In practice, the position of the shock z_s is estimated by detecting the maximum of the gradient of axial velocity. The power spectral densities of the time variations of the position of the shock are then computed. The results obtained for $r = 0$ and $r = 0.85r_0$ are represented in Figure 15. The frequencies of the peaks in the near-nozzle pressure spectra for the two first azimuthal modes are also plotted. On the jet axis at $r = 0$, where only the axisymmetric mode is present, two peaks are observed in the spectrum at $St = 0.05$ and 0.09 . The frequency of the second peak is the same as that of the second near-nozzle peak for $n_\theta = 0$. Closer to the mixing layer, the spectrum for $r = 0.85r_0$ exhibits three peaks at $St = 0.03$, 0.09 and 0.16 . The second and third peak frequencies are similar to those of the second near-nozzle peaks for $n_\theta = 0$ and $n_\theta = 1$, respectively. This result suggests that the high-frequency peaks in the near-nozzle pressure spectrum are linked to the motions of the near-plate shock.

4 Conclusion

In this paper, the presence and properties of acoustic peaks near the nozzle of impinging rocket jets have been investigated using large-eddy simulations for nozzle-to-plate distances varying from 15 to 30 nozzle radii. For all distances, peaks are found to emerge weakly in the near-nozzle pressure spectra. The weak emergence of the peaks for all nozzle-to-plate distances indicates that no intense feedback mechanism establishes between the nozzle and the plate, even for $L = 15r_0$. The absence of strong resonance is likely due to the jet high Mach number, as the growth rate of the Kelvin–Helmholtz waves, forming the downstream part of possible feedback loops, decreases as the jet Mach number increases [48, 49]. In further works, this growth rate could be investigated. Regarding the peak frequencies, they do not vary much with the nozzle-to-plate distance. Similarly to the frequencies of the tones obtained in the near-nozzle pressure fields of jets at lower Mach numbers, they are located inside or near the allowable frequency ranges of the upstream-propagating guided jet waves, indicating a

link with these waves for rocket jets. As for the sound levels, they increase as the plate is closer to the nozzle exit. For the shortest nozzle-to-plate distance, a normal shock is found near the plate, creating additional sound waves by a shock-leakage mechanism. This shock is found to oscillate at frequencies close to those of peaks in the near-nozzle pressure spectra.

Conflict of interest

The authors declare no conflict of interest.

Acknowledgments

This work was financed by the IRICE IJES project RA0014963 (Installed Jet Effect Simulator, FEDER-FSE Rhône-Alpes). It was granted access to the HPC resources of PMCS2I (Pôle de Modélisation et de Calcul en Sciences de l'Ingénieur et de l'Information) of Ecole Centrale de Lyon, PSMN (Pôle Scientifique de Modélisation Numérique) of ENS de Lyon, members of FLMSN (Fédération Lyonnaise de Modélisation et Sciences Numériques), partner of EQUIPEX EQUIP@MESO, and to the resources of IDRIS (Institut du Développement et des Ressources en Informatique Scientifique) under the allocation 2021-2a0204 made by GENCI (Grand Equipement National de Calcul Intensif). It was performed within the framework of the LABEX CeLyA (ANR-10-LABX-0060) of Université de Lyon, within the program Investissements d'Avenir (ANR-16-IDEX-0005) operated by the French National Research Agency (ANR).

References

1. C.P. Lubert, K.L. Gee, S. Tsutsumi: Supersonic jet noise from launch vehicles: 50 years since nasa sp-8072. *Journal of the Acoustical Society of America* 151, 2 (2022) 752–791.
2. A. Powell: On edge tones and associated phenomena. *Acta Acustica United with Acustica* 3, 4 (1953) 233–243.
3. G. Neuwerth: Acoustic feedback of a subsonic and supersonic free jet which impinges on an obstacle. NASA Technical Translation No. F-15719, 1974.
4. J.S. Preisser: Fluctuating surface pressure and acoustic radiation for subsonic normal jet impingement. NASA Technical Paper 1361, 1979.
5. C.-M. Ho, N.S. Nasseir: Dynamics of an impinging jet. Part 1. The feedback phenomenon. *Journal of Fluid Mechanics* 105 (1981) 119–142.
6. N.S. Nasseir, C.-M. Ho: Dynamics of an impinging jet. Part 2. The noise generation. *Journal of Fluid Mechanics* 116 (1982) 379–391.
7. V. Jaunet, M. Mancinelli, P. Jordan, A. Towne, D.M. Edgington-Mitchell, G. Lehnasch, S. Girard: Dynamics of round jet impingement. AIAA Paper 2019–2769, 2019.
8. M. Varé, C. Bogey: Generation of acoustic tones in round jets at a Mach number of 0.9 impinging on a plate with and without a hole. *Journal of Fluid Mechanics* 936 (2022) A16.
9. T.D. Norum: Supersonic rectangular jet impingement noise experiments. *AIAA Journal* 29, 7 (1991) 1051–1057.
10. A. Krothapalli, E. Rajkuperan, F. Alvi, L. Lourenco: Flow field and noise characteristics of a supersonic impinging jet. *Journal of Fluid Mechanics* 392 (1999) 155–181.
11. B. Henderson, J. Bridges, M. Wernet: An experimental study of the oscillatory flow structure of tone-producing supersonic impinging jets. *Journal of Fluid Mechanics* 542 (2005) 115–137.
12. A. Risborg, J. Soria: High-speed optical measurements of an underexpanded supersonic jet impinging on an inclined plate, in: 28th International Congress on High-Speed Imaging and Photonics, Vol. 7126, International Society for Optics and Photonics, 2009, p. 71261F.
13. N.A. Buchmann, D.M. Mitchell, K.M. Ingvorsen, D.R. Honnery, J. Soria: High spatial resolution imaging of a supersonic underexpanded jet impinging on a flat plate, in: 6th Australian Conference on Laser Diagnostics in Fluid Mechanics and Combustion, 2011.
14. D.M. Mitchell, D.R. Honnery, J. Soria: The visualization of the acoustic feedback loop in impinging underexpanded supersonic jet flows using ultra-high frame rate schlieren. *Journal of Visualization* 15, 4 (2012) 333–341.
15. A. Dauplain, L.Y. Gicquel, S. Moreau: Large-eddy simulation of supersonic impinging jets. *AIAA Journal* 50, 7 (2012) 1560–1574.
16. R. Gojon, C. Bogey, O. Marsden: Investigation of tone generation in ideally expanded supersonic planar impinging jets using large-eddy simulation. *Journal of Fluid Mechanics* 808 (2016) 90–115.
17. C. Bogey, R. Gojon: Feedback loop and upwind-propagating waves in ideally expanded supersonic impinging round jets. *Journal of Fluid Mechanics* 823 (2017) 562–591.
18. R. Gojon, C. Bogey: Flow structure oscillations and tone production in underexpanded impinging round jets. *AIAA Journal* 55, 6 (2017) 1792–1805.
19. A. Towne, A.V.G. Cavalieri, P. Jordan, T. Colonius, O. Schmidt, V. Jaunet, G.A. Brès: Acoustic resonance in the potential core of subsonic jets. *Journal of Fluid Mechanics* 825 (2017) 1113–1152.
20. O.T. Schmidt, A. Towne, T. Colonius, A.V.G. Cavalieri, P. Jordan, G.A. Brès: Wavepackets and trapped acoustic modes in a turbulent jet: coherent structure eduction and global stability. *Journal of Fluid Mechanics* 825 (2017) 1153–1181.
21. C. Bogey: Acoustic tones in the near-nozzle region of jets: characteristics and variations between Mach numbers 0.5 and 2. *Journal of Fluid Mechanics* 921 (2021) A3.
22. S. Kawai, S. Tsutsumi, R. Takaki, K. Fujii: Computational aeroacoustic analysis of overexpanded supersonic jet impingement on a flat plate with/without hole, in: ASME/JSME 2007 5th Joint Fluids Engineering Conference, American Society of Mechanical Engineers, 2007, pp. 1163–1167.
23. S. Tsutsumi, R. Takaki, H. Ikaida, K. Terashima: Numerical aeroacoustics analysis of a scaled solid jet impinging on flat plate with exhaust hole, in: 30th International Symposium on Space Technology and Science, 2015.
24. J. Troyes, F. Vuillot, A. Langenais, H. Lambaré: Coupled CFD-CAA simulation of the noise generated by a hot supersonic jet impinging on a flat plate with exhaust hole. AIAA Paper 2019–2752, 2019.
25. M. Varé, C. Bogey: Flow and acoustic fields of rocket jets impinging on a perforated plate, *AIAA Journal* 60 (2022) 1–14.
26. C. Bogey, O. Marsden, C. Bailly: Large-eddy simulation of the flow and acoustic fields of a Reynolds number 10^5 subsonic jet with tripped exit boundary layers. *Physics of Fluids* 23, 3 (2011) 035104.
27. C. Bogey, C. Bailly: A family of low dispersive and low dissipative explicit schemes for flow and noise computations. *Journal of Computational Physics* 194, 1 (2004) 194–214.

28. C. Bogey, N. De Cacqueray, C. Bailly: A shock-capturing methodology based on adaptative spatial filtering for high-order non-linear computations. *Journal of Computational Physics* 228, 5 (2009) 1447–1465.
29. D. Fauconnier, C. Bogey, E. Dick: On the performance of relaxation filtering for large-eddy simulation. *Journal of Turbulence* 14, 1 (2013) 22–49.
30. C.K.W. Tam, Z. Dong: Radiation and outflow boundary conditions for direct computation of acoustic and flow disturbances in a non uniform mean flow. *Journal of Computational Acoustics* 4, 02 (1996) 175–201.
31. K. Mohseni, T. Colonius: Numerical treatment of polar coordinate singularities. *Journal of Computational Physics* 157, 2 (2000) 787–795.
32. S. Viazzo, A. Dejoan, R. Schiestel: Spectral features of the wall-pressure fluctuations in turbulent wall flows with and without perturbations using les. *International Journal of Heat and Fluid Flow* 22, 1 (2001) 39–52.
33. P. Schlatter, Q. Li, G. Brethouwer, A.V. Johansson, D.S. Henningson: Simulations of spatially evolving turbulent boundary layers up to $Re_\theta=4300$. *International Journal of Heat and Fluid Flow* 31, 3 (2010) 251–261.
34. X. Gloerfelt, J. Berland: Turbulent boundary-layer noise: direct radiation at Mach number 0.5. *Journal of Fluid Mechanics* 723 (2013) 318–351.
35. F. Kremer, C. Bogey: Large-eddy simulation of turbulent channel flow using relaxation filtering: Resolution requirement and Reynolds number effects. *Computers & Fluids* 116 (2015) 17–28.
36. N. De Cacqueray, C. Bogey, C. Bailly: Investigation of a high-Mach-number overexpanded jet using large-eddy simulation. *AIAA Journal* 49, 10 (2011) 2171–2182.
37. A. Langenais, F. Vuillot, J. Troyes, C. Bailly: Accurate simulation of the noise generated by a hot supersonic jet including turbulence tripping and nonlinear acoustic propagation. *Physics of Fluids* 31, 1 (2019) 016105.
38. T. Nonomura, K. Fujii: Overexpansion effects on characteristics of Mach waves from a supersonic cold jet. *AIAA Journal* 49, 10 (2011) 2282–2294.
39. P. Pineau, C. Bogey: Steepened Mach waves near supersonic jets: study of azimuthal structure and generation process using conditional averages. *Journal of Fluid Mechanics* 880 (2019) 594–619.
40. C.K.W. Tam, K.K. Ahuja: Theoretical model of discrete tone generation by impinging jets. *Journal of Fluid Mechanics* 214 (1990) 67–87.
41. B. Henderson: The connection between sound production and jet structure of the supersonic impinging jet. *Journal of the Acoustical Society of America* 111, 2 (2002) 735–747.
42. G. Sinibaldi, L. Marino, G.P. Romano: Sound source mechanisms in under-expanded impinging jets. *Experiments in Fluids* 56, 5 (2015) 105.
43. T. Nonomura, H. Honda, Y. Nagata, M. Yamamoto, S. Morizawa, S. Obayashi, K. Fujii: Plate-angle effects on acoustic waves from supersonic jets impinging on inclined plates. *AIAA Journal* 54, 3 (2016) 816–827.
44. C. Brehm, J.A. Housman, C.C. Kiris: Noise generation mechanisms for a supersonic jet impinging on an inclined plate. *Journal of Fluid Mechanics* 797 (2016) 802–850.
45. T. Suzuki, S.K. Lele: Shock leakage through an unsteady vortex-laden mixing layer: application to jet screech. *Journal of Fluid Mechanics* 490 (2003) 139–167.
46. J. Berland, C. Bogey, C. Bailly: Numerical study of screech generation in a planar supersonic jet. *Physics of Fluids* 19, 7 (2007) 075105.
47. D. Edgington-Mitchell, J. Weightman, S. Lock, R. Kirby, V. Nair, J. Soria, D. Honnery: The generation of screech tones by shock leakage. *Journal of Fluid Mechanics* 908 (2021) A46.
48. A. Michalke: Survey on jet instability theory. *Progress in Aerospace Sciences* 21 (1984) 159–199.
49. P.J. Morris: The instability of high speed jets. *International Journal of Aeroacoustics* 9, 1–2 (2010) 1–50.

Cite this article as: Varé M. & Bogey C. 2022. Presence and properties of acoustic peaks near the nozzle of impinging rocket jets. *Acta Acustica*, 6, 36.